



Article

Modeling and Performance Evaluation of Precise Positioning and Time-Frequency Transfer with Galileo Five-Frequency Observations

Wei Xu ^{1,2} , Wen-Bin Shen ^{1,2,3,*} , Cheng-Hui Cai ^{1,2} , Li-Hong Li ^{1,2}, Lei Wang ^{1,2} and Zi-Yu Shen ⁴

¹ School of Geodesy and Geomatics, Wuhan University, Wuhan 430079, China; whuxwei@whu.edu.cn (W.X.); chcai@whu.edu.cn (C.-H.C.); sggllh@whu.edu.cn (L.-H.L.); lwangsgg@whu.edu.cn (L.W.)

² Time and Frequency Geodesy Center, Wuhan University, Wuhan 430079, China

³ State Key Laboratory of Information Engineering in Surveying, Mapping and Remote Sensing, Wuhan University, Wuhan 430079, China

⁴ School of Resource, Environmental Science and Engineering, Hubei University of Science and Technology, Xianning 437100, China; zyshen@hbust.edu.cn

* Correspondence: wbshen@sgg.whu.edu.cn; Tel.: +86-27-6877-1539

Abstract: The present Global Navigation Satellite System (GNSS) can provide at least double-frequency observations, and especially the Galileo Navigation Satellite System (Galileo) can provide five-frequency observations for all constellation satellites. In this contribution, precision point positioning (PPP) models with Galileo E1, E5a, E5b, E5 and E6 frequency observations are established, including a dual-frequency (DF) ionospheric-free (IF) combination model, triple-frequency (TF) IF combination model, quad-frequency (QF) IF combination model, four five-frequency (FF) IF combination models and an FF uncombined (UC) model. The observation data of five stations for seven days are selected from the multi-GNSS experiment (MGEX) network, forming four time-frequency links ranging from 454.6 km to 5991.2 km. The positioning and time-frequency transfer performances of Galileo multi-frequency PPP are compared and evaluated using GBM (which denotes precise satellite orbit and clock bias products provided by Geo Forschung Zentrum (GFZ)), WUM (which denotes precise satellite orbit and clock bias products provided by Wuhan University (WHU)) and GRG (which denotes precise satellite orbit and clock bias products provided by the Centre National d'Études Spatiales (CNES)) precise products. The results show that the performances of the DF, TF, QF and FF PPP models are basically the same, the frequency stabilities of most links can reach $\text{sub}10^{-16}$ level at 120,000 s, and the average three-dimensional (3D) root mean square (RMS) of position and average frequency stability (120,000 s) can reach 1.82 cm and 1.18×10^{-15} , respectively. The differences of 3D RMS among all models are within 0.17 cm, and the differences in frequency stabilities (in 120,000 s) among all models are within 0.08×10^{-15} . Using the GRG precise product, the solution performance is slightly better than that of the GBM or WUM precise product, the average 3D RMS values obtained using the WUM and GRG precise products are 1.85 cm and 1.77 cm, respectively, and the average frequency stabilities at 120,000 s can reach 1.13×10^{-15} and 1.06×10^{-15} , respectively.

Keywords: Galileo; five-frequency; PPP; positioning; time-frequency transfer



Citation: Xu, W.; Shen, W.-B.; Cai, C.-H.; Li, L.-H.; Wang, L.; Shen, Z.-Y. Modeling and Performance Evaluation of Precise Positioning and Time-Frequency Transfer with Galileo Five-Frequency Observations. *Remote Sens.* **2021**, *13*, 2972. <https://doi.org/10.3390/rs13152972>

Academic Editor: Shuanggen Jin

Received: 24 June 2021

Accepted: 25 July 2021

Published: 28 July 2021

Publisher's Note: MDPI stays neutral with regard to jurisdictional claims in published maps and institutional affiliations.



Copyright: © 2021 by the authors. Licensee MDPI, Basel, Switzerland. This article is an open access article distributed under the terms and conditions of the Creative Commons Attribution (CC BY) license (<https://creativecommons.org/licenses/by/4.0/>).

1. Introduction

In recent decades, Global Navigation Satellite System (GNSS) have made great progress, including Global Positioning System (GPS) modernization by the USA, the BeiDou Navigation Satellite System (BDS) developed by China, the Galileo Navigation Satellite System (Galileo) constructed by the European Union (UN), the Global Navigation Satellite System in Russia (GLONASS) restored by Russia, and the Quasi-Zenith Satellite System (QZSS) implemented by Japan, which have realized interoperability and multi-frequency signal support [1–5]. The Galileo system operated by the European Space

Agency (ESA) supports all satellite broadcasts of E1 (1575.42 MHz), E5a (1176.45 MHz), E5b (1207.14 MHz), E5 (1191.795 MHz) and E6 (1278.75 MHz) five-frequency signals throughout the constellation to provide positioning, navigation, and timing (PNT) services worldwide [6,7]. Galileo multifrequency signals have improved capacity redundancy and reliability, have provided more opportunities in low-noise combination, cycle-slip detection, and repair [8,9], ambiguity resolution [10], positioning [7,11], time-frequency transfer [12] and other aspects, and have faced more challenges of inter frequency bias (*IFB*), which represents significant development potential.

With the support of the precise ephemeris and clock products provided by IGS Analysis Centers (ACs), precise point positioning (PPP) technology has gradually become a popular research topic due to its characteristics of high precision and flexible operation and has been widely used in the field of geosciences and time-frequency transfer [13,14]. The PPP technique has been adopted by the Bureau International des Poids et Mesures (BIPM) and many other international laboratories for international atomic time (TAI) maintenance applications since 2009 [15,16].

Many scholars have investigated the performance of Galileo multifrequency signals in positioning, timing, and orbit determination. Duong et al. [17] proved the multifrequency advantage of PPP ambiguity resolution (AR) and found that the four-frequency Galileo combination of E1/E5a/E5b/E6 provides the lowest geometric and ambiguity variance. Tu et al. [18] studied the performance of real-time kinematics (RTK) using Galileo four-frequency observations, and the results showed that multiple frequencies were much better than single-frequency, and the coordinates' standard deviation (STD) was improved by approximately 30%. Liu et al. [19] proposed the method of PPP uncombined (UC) AR by using Galileo triple-frequency observations. Qin et al. [20] investigated Galileo precise time transfer with the COM (which denotes precise satellite orbit and clock bias products provided by Center for Orbit Determination in Europe (CODE)), WUM (which denotes precise satellite orbit and clock bias products provided by Wuhan University (WHU)), GRM (which denotes multi GNSS precise satellite orbit and clock bias products provided by Centre National d'Etudes Spatiales (CNES)), SHA (which denotes precise satellite orbit and clock bias products provided by Shanghai Astronomical Observatory (SHAO)), and GBM (which denotes precise satellite orbit and clock bias products provided by Geo Forschungs Zentrum (GFZ)) final products and CLK93 (which denotes real-time (RT) precise satellite orbit and clock bias products provided by CNES) RT products. Li et al. [21] proved the superiority of the Galileo five-frequency signal in PPP rapid ambiguity solutions compared with dual-frequency and triple-frequency solutions. Zhang et al. [22] focused on the Galileo quad-frequency PPP time and transfer performance with E1, E5a, E5b and E5 observations. Liu et al. [23] used the phase bias product provided by CNES to test triple-frequency GPS/Galileo RT PPP AR and proved that triple-frequency PPP AR can improve the convergence time performance and positioning accuracy compared with dual-frequency PPP AR. Kuang et al. [24] studied RT UC orbit determination using Galileo triple-frequency observations and the characteristics of satellite inter frequency clock bias (IFCB). Su and Jin [25] analyzed the receiver clock, tropospheric delay, receiver IFBs and differential code bias (*DCB*) of combined and UC five-frequency PPP models and proved the consistency of several models.

Jin and Su [26] presented and evaluated PPP models using the single-, dual-, triple-, and quad-frequency BDS observations, and the results show that the multi-frequency BDS observations will greatly improve the PPP performances. Ge et al. [27] proved that quad-frequency BDS-3 or Galileo PPP models could be used to time transfer, the stability and accuracy of quad-frequency and dual-frequency *IF* model are the same.

Previous studies focused more on Galileo dual-frequency (DF), triple-frequency (TF) and quad-frequency (QF) precise positioning but less on five-frequency (FF) precise positioning and precise time-frequency transfer. The contribution of this work is that we established multiple *IF* and UC PPP mathematical models with Galileo five frequency observations, and provided the processing method and specific formula of *IFB* parameters

in the multi-frequency PPP model. In addition, based on the evaluation the multipath combination noise of Galileo multi-frequency observations, the convergence time and positioning accuracy of DF, TF, QF and FF models were evaluated by using precision products of different ACs, and the performance of time-frequency transfer of Galileo E1, E5a, E5b, E5 and E6 multi frequency signals is compared and analyzed systematically for the first time. In Section 2, five mathematical PPP models of the Galileo E1, E5a, E5b, E5 and E6 frequency observations are established; observation types, combination coefficients, ionospheric coefficients and noise amplification coefficients of the Galileo DF, TF, QF, and FF PPP models are also summarized and compared. Section 3 introduces the experimental data and their processing strategy. In Section 4, we use the GBM, WUM and GRG (which denote precise satellite orbit and clock bias products provided by the Centre National d'Etudes Spatiales (CNES)) precise products to evaluate the positioning and the time-frequency transfer performance results of the Galileo DF, TF, QF, and FF PPP models. Finally, we summarize this work and draw some conclusions.

2. Methodology

In this section, starting from GNSS raw observations, the Galileo FF UC PPP model, the single ionosphere-free (IF) PPP model among five frequency observations, two QF IF PPP model among five frequency observations, three TF IF PPP model among five frequency observations and four DF IF PPP model among five frequency observations are established, respectively. Then, the observation types, combination coefficients, ionospheric coefficients and noise amplification coefficients of the Galileo DF, TF, QF, and FF PPP models are summarized and compared.

2.1. GNSS Observation Model

GNSS pseudo range and carrier phase observations can be expressed as [28]:

$$\begin{cases} P_{r,j}^i = \rho_r^i + cdt_r - cdt^i + MF_r^i ZWD_r + \gamma_j I_{r,1}^i + d_{r,j} - d_j^i + \zeta_j^i \\ L_{r,j}^i = \rho_r^i + cdt_r - cdt^i + MF_r^i ZWD_r - \gamma_j I_{r,1}^i + \lambda_j (N_j^i + b_{r,j} - b_j^i) + \xi_j^i \end{cases} \quad (1)$$

where the P and L denote pseudo range and carrier phase observation values in meters, respectively; superscript i denotes the i -th satellite of the GNSS system; subscripts r and j denote the receiver and frequency identifiers, respectively; for convenience, the frequency identifiers 1, 2, 3, 4 and 5 in the Galileo system represent E1, E5a, E5b, E5 and E6 frequencies, respectively; λ is wavelength corresponding to frequency j ; ρ represents the geometric distance between the satellite and receiver; c represents the speed of light in a vacuum; dt_r and dt^s denote receiver and satellite clock offsets in seconds, respectively; MF denotes the wet mapping function; ZWD is zenith troposphere wet delay (ZWD); I denotes the slant ionospheric delay; γ_j denotes frequency dependent ionospheric delay amplification factors, $\gamma_j = \lambda_j^2 / \lambda_1^2$; N is carrier phase integer ambiguity; d denotes the receiver uncalibrated code delay (UCD) in meters; b denotes uncalibrated phase delay (UPD) in cycles; and ζ and ξ represent the pseudo range and carrier phase observation noises, respectively.

Defining the notations:

$$\begin{cases} \alpha_{mn} = (f_m)^2 / [(f_m)^2 - (f_n)^2] \\ \beta_{mn} = -(f_n)^2 / [(f_m)^2 - (f_n)^2] \\ DCB_{r,mn} = d_{r,m} - d_{r,n} \end{cases} \quad (2)$$

where α_{mn} and β_{mn} are IF combination frequency factors ($m, n = 1, 2, 3, 4, 5; m \neq n$).

2.2. Five-Frequency UC PPP Model

In the five-frequency UC PPP model, the ionospheric delay is related to E1/E5a IF combined with DCB and cannot be separated, and the IFB parameters are required to

compensate for the inconsistency of receiver UCDs at the E5b, E5 and E6 frequencies. Then, the Galileo five-frequency UC pseudo range and carrier phase observations can be expressed as:

$$\begin{cases} p_{r,j}^i = \boldsymbol{\mu}_r^i \cdot \mathbf{x} + c\tilde{d}t_r + MF_r^i ZWD_r + \gamma_j \tilde{I}_{r,j}^i + \zeta_j^i & (j = 1, 2) \\ p_{r,j}^i = \boldsymbol{\mu}_r^i \cdot \mathbf{x} + c\tilde{d}t_r + MF_r^i ZWD_r + IFB_{UC_j} + \gamma_j \tilde{I}_{r,1}^i + \zeta_j^i & (j = 3, 4, 5) \\ l_{r,j}^i = \boldsymbol{\mu}_r^i \cdot \mathbf{x} + c\tilde{d}t_r + MF_r^i ZWD_r - \gamma_j \tilde{I}_{r,1}^i + \lambda_j \tilde{N}_j^i + \tilde{\zeta}_j^i & (j = 1, 2, 3, 4, 5) \end{cases} \quad (3)$$

with

$$\begin{cases} c\tilde{d}t_r = cdt_r + d_{r,IF12} \\ \tilde{I}_{r,1}^i = I_{r,1}^i + DCB_{r,12} / (1 - \gamma_2) \\ IFB_{UC_j} = d_{r,j} - d_{r,IF12} - \gamma_j DCB_{r,12} / (1 - \gamma_j) & (j = 3, 4, 5) \\ \lambda_j \tilde{N}_j^i = \lambda_j (N_j + b_{r,j} - b_j^i) - d_{IF12}^i - d_{r,IF12} + \gamma_j DCB_{r,12} / (1 - \gamma_j) & (j = 1, 2, 3, 4, 5) \end{cases} \quad (4)$$

where p and l are pseudo range and carrier phase observed minus computed (OMC) values in meters, respectively; subscript IF denotes ionospheric-free combination; $DCB_{r,12}$ denotes E1 and E5a DCB of the receiver side; IFB_{uc} denotes UC IFBs; $\boldsymbol{\mu}$ denotes the unit vector of the component from the receiver to the satellites; \mathbf{x} denotes the vector of the receiver position increments; and hat “ \sim ” denotes the reparametrized estimate.

2.3. Single Five-Frequency IF Combination (FF1) PPP Model

Galileo five-frequency observations can be combined according to the geometry-free, ionospheric-free and minimum noise principles with a single ionospheric combination observation and can be expressed as:

$$\begin{cases} e_1 + e + 2e_3 + e_4 + e_5 = 1 \\ e_1 \gamma_1 + e \gamma_2 + e_3 \gamma_3 + e_4 \gamma_4 + e_5 \gamma_5 = 0 \\ e_1^2 + e_2^2 + e_3^2 + e_4^2 + e_5^2 = \min \end{cases} \quad (5)$$

The coefficients following the above criteria can be uniquely determined as [25]:

$$\begin{cases} e_1 = (\gamma_2 + \gamma_3 + \gamma_4 + \gamma_5 - \gamma_2^2 - \gamma_3^2 - \gamma_4^2 - \gamma_5^2) / e \\ e_2 = (\gamma_2 + \gamma_2 \gamma_3 + \gamma_2 \gamma_4 + \gamma_2 \gamma_5 - 1 - \gamma_3^2 - \gamma_4^2 - \gamma_5^2) / e \\ e_3 = (\gamma_3 + \gamma_2 \gamma_3 + \gamma_3 \gamma_4 + \gamma_3 \gamma_5 - 1 - \gamma_2^2 - \gamma_4^2 - \gamma_5^2) / e \\ e_4 = (\gamma_4 + \gamma_2 \gamma_4 + \gamma_3 \gamma_4 + \gamma_4 \gamma_5 - 1 - \gamma_2^2 - \gamma_3^2 - \gamma_5^2) / e \\ e_5 = (\gamma_5 + \gamma_2 \gamma_5 + \gamma_3 \gamma_5 + \gamma_4 \gamma_5 - 1 - \gamma_2^2 - \gamma_3^2 - \gamma_4^2) / e \end{cases} \quad (6)$$

with

$$e = -(\gamma_2 - 1)^2 - (\gamma_3 - 1)^2 - (\gamma_4 - 1)^2 - (\gamma_5 - 1)^2 - (\gamma_3 - \gamma_2)^2 - (\gamma_4 - \gamma_2)^2 - (\gamma_5 - \gamma_2)^2 - (\gamma_4 - \gamma_3)^2 - (\gamma_5 - \gamma_3)^2 - (\gamma_5 - \gamma_4)^2 \quad (7)$$

where e_1, e_2, e_3, e_4 and e_5 denote the five-frequency IF combination coefficients, e is the coefficient in the denominator.

When the five pseudo range measurements are combined within a single equation, the FF1 PPP observation equation can be expressed as:

$$\begin{cases} p_{r,IF12345}^i = \boldsymbol{\mu}_r^i \cdot \mathbf{x} + c\tilde{d}t_r + MF_r^i ZWD_r + \zeta_{IF12345}^i \\ l_{r,IF12345}^i = \boldsymbol{\mu}_r^i \cdot \mathbf{x} + c\tilde{d}t_r + MF_r^i ZWD_r + \lambda_{IF12345} \tilde{N}_{IF12345}^i + \tilde{\zeta}_{IF12345}^i \end{cases} \quad (8)$$

with

$$\begin{cases} c\tilde{d}t_r = cdt_r + d_{r,IF12345} \\ \lambda_{IF12345} \tilde{N}_{IF12345}^i = \lambda_{IF12345}^i (N_{IF12345}^i + b_{r,IF12345} - b_{IF12345}^i) - d_{IF12}^i - d_{r,IF12345} \end{cases} \quad (9)$$

where the receiver clock offset will absorb the UCD of E1/E5a/E5b/E5/E6 *IF* combination.

2.4. Two Quad-Frequency *IF* Combinations (FF2) PPP Model

In the FF2 PPP model, E1/E5a/E5b/E5 and E1/E5a/E5b/E6 observations were selected to form two quad-frequency *IF* combinations. Similarly, additional *IFB* parameters were required to maintain compatibility between the two quad-frequency *IF* combinations. Hence, the two quad-frequency *IF* combination PPP models can be formulated as follows:

$$\begin{cases} p_{r,IF_{1234}}^i = \mu_r^i \cdot \mathbf{x} + c\tilde{d}t_r + MF_r^i ZWD_r + \zeta_{IF_{1234}}^i \\ p_{r,IF_{123j}}^i = \mu_r^i \cdot \mathbf{x} + c\tilde{d}t_r + MF_r^i ZWD_r + IFB_{IF_{123j}}^i + \zeta_{IF_{123j}}^i \quad (j = 5) \\ l_{r,IF_{123j}}^i = \mu_r^i \cdot \mathbf{x} + c\tilde{d}t_r + MF_r^i ZWD_r + \lambda_{IF_{123j}} \tilde{N}_{IF_{1234}}^i + \zeta_{IF_{123j}}^i \quad (j = 4, 5) \end{cases} \quad (10)$$

with

$$\begin{cases} c\tilde{d}t_r = cdt_r + d_{r,IF_{1234}} \\ IFB_{IF_{123j}}^i = d_{r,IF_{123j}} - d_{r,IF_{1234}} \quad (j = 5) \\ \lambda_{IF_{123j}} \tilde{N}_{IF_{123j}}^i = \lambda_{IF_{123j}} (N_{IF_{123j}}^i + b_{r,IF_{123j}} - b_{IF_{123j}}^i) - d_{IF_{12}}^i - d_{r,IF_{1234}} \quad (j = 4, 5) \end{cases} \quad (11)$$

where $IFB_{IF_{1235}}$ denotes the *IFB* parameters between the E1/E5a/E5b/E6 and E1/E5a/E5b/E6 code *IF* combinations.

2.5. Three Triple-Frequency *IF* Combinations (FF3) PPP Model

The FF3 PPP model for the Galileo five-frequency was implemented by combining the three triple-frequency *IF* observations, and we chose E1/E5a/E5b, E1/E5a/E5 and E1/E5a/E6 observations for combination. In this case, we needed to add two estimated *IFB* parameters, which can be expressed as:

$$\begin{cases} p_{r,IF_{123}}^i = \mu_r^i \cdot \mathbf{x} + c\tilde{d}t_r + MF_r^i ZWD_r + \zeta_{IF_{123}}^i \\ p_{r,IF_{12j}}^i = \mu_r^i \cdot \mathbf{x} + c\tilde{d}t_r + MF_r^i ZWD_r + IFB_{IF_{12j}}^i + \zeta_{IF_{12j}}^i \quad (j = 4, 5) \\ l_{r,IF_{12j}}^i = \mu_r^i \cdot \mathbf{x} + c\tilde{d}t_r + MF_r^i ZWD_r + \lambda_{IF_{12j}} \tilde{N}_{IF_{12j}}^i + \zeta_{IF_{12j}}^i \quad (j = 3, 4, 5) \end{cases} \quad (12)$$

with

$$\begin{cases} c\tilde{d}t_r = cdt_r + d_{r,IF_{123}} \\ IFB_{IF_{12j}}^i = d_{r,IF_{12j}} - d_{r,IF_{123}} \quad (j = 4, 5) \\ \lambda_{IF_{12j}} \tilde{N}_{IF_{12j}}^i = \lambda_{IF_{12j}} (N_{IF_{12j}}^i + b_{r,IF_{12j}} - b_{IF_{12j}}^i) - d_{IF_{12}}^i - d_{r,IF_{12j}} \quad (j = 3, 4, 5) \end{cases} \quad (13)$$

where $IFB_{IF_{124}}$ and $IFB_{IF_{125}}$ denote the *IFB* parameters between the E1/E5a/E5b, E1/E5a/E6 and E1/E5a/E5b code *IF* combinations.

2.6. Four Dual-Frequency *IF* Combinations (FF4) PPP Model

The FF4 PPP model consists of the observation equation implemented by combining the four DF *IF* observations. Theoretically, any two Galileo E1, E5a, E5b, E5, and E6 signals can form a dual-frequency ionospheric-free combination. However, considering the noise amplification coefficients after combination, we chose E1/E5a, E1/E5b, E1/E5 and E1/E6 signals for combination. In addition, it was necessary to note that the clock difference of each combination is not consistent. In this case, we needed to add estimated *IFB* parameters, which can be expressed as:

$$\begin{cases} p_{r,IF_{12}}^i = \mu_r^i \cdot \mathbf{x} + c\tilde{d}t_r + MF_r^i ZWD_r + \zeta_{IF_{12}}^i \\ p_{r,IF_{1j}}^i = \mu_r^i \cdot \mathbf{x} + c\tilde{d}t_r + MF_r^i ZWD_r + IFB_{IF_{1j}}^i + \zeta_{IF_{1j}}^i \quad (j = 3, 4, 5) \\ l_{r,IF_{1j}}^i = \mu_r^i \cdot \mathbf{x} + c\tilde{d}t_r + MF_r^i ZWD_r + \lambda_{IF_{1j}} \tilde{N}_{IF_{1j}}^i + \zeta_{IF_{1j}}^i \quad (j = 2, 3, 4, 5) \end{cases} \quad (14)$$

with

$$\begin{cases} c\tilde{d}t_r = cdt_r + d_{r,IF12} \\ IFB_{IF1j} = (d_{r,j} - d_{r,1}\gamma_j) / (1 - \gamma_j) - d_{r,IF12} \quad (j = 3, 4, 5) \\ \lambda_{IF1j} \tilde{N}_{IF1j}^i = \lambda_{IF1j} (N_{r,IF1j}^i + b_{r,IF1j} - b_{IF1j}^i) - d_{IF12}^i - d_{r,IF12} \quad (j = 2, 3, 4, 5) \end{cases} \quad (15)$$

where IFB_{IF13} , IFB_{IF14} and IFB_{IF15} denote the IFB parameters between the E1/E5b, E1/E5, E1/E6 and E1/E5a code IF combinations.

2.7. Comparison of Galileo Five Frequency PPP Models

Table 1 summarizes the types of observation values, combination coefficients, ionospheric delay coefficients and noise amplification coefficients of the dual-frequency, triple-frequency, quad-frequency, and five-frequency PPP models. Among them, the FF2, FF3 and FF4 PPP models are composed of DF, TF and QF IF combinations, and additional IFB parameters need to be estimated to maintain consistency among different equations. The noise amplification factor of FF1 is smaller than that of other IF combinations. After the filter converges and the ionosphere and ambiguity parameters are separated, the FF1, FF2, FF3, FF4 and UC PPP models are equivalent.

Table 1. Summarization of Galileo DF, TF, QF and FF PPP models.

Models	Observed Type	E1	E5a	E5b	E5	E6	Ion	Noise
DF	E1/E5a	2.261	−1.261	/	/	/	/	2.588
TF	E1/E5a/E5b	2.315	−0.836	−0.479	/	/	/	2.507
QF	E1/E5a/E5b/E5	2.317	−0.606	−0.274	−0.437	/	/	2.450
FF1	E1/E5a/E5b/E5/E6	2.217	−0.680	−0.351	−0.512	0.326	/	2.423
FF2	E1/E5a/E5b/E5	2.317	−0.606	−0.274	−0.437	/	/	2.450
	E1/E5a/E5b/E6	2.255	−0.904	−0.545	0.193	/	/	2.497
FF3	E1/E5a/E5b	2.315	−0.836	−0.479	/	/	/	2.507
	E1/E5a/E5	2.293	0.734	−0.559	/	/	/	2.471
	E1/E5a/E6	2.269	−1.244	−0.024	/	/	/	2.588
FF4	E1/E5a	2.261	−1.261	/	/	/	/	2.588
	E1/E5b	2.422	/	−1.422	/	/	/	2.809
	E1/E5	2.338	/	/	−1.338	/	/	2.694
	E1/E6	2.931	/	/	/	−1.931	/	3.510
UC	E1	1.000	/	/	/	/	1.000	1.000
	E5a	/	1.000	/	/	/	1.793	1.000
	E5b	/	/	1.000	/	/	1.703	1.000
	E5	/	/	/	1.000	/	1.747	1.000
	E6	/	/	/	/	1.000	1.518	1.000

2.8. Date Selection and Processing Strategies

Five stations that can receive the Galileo E1/E5a/E5b/E5/E6 signal observations over a period of 190–196 days in 2020 were selected from the international GNSS service (IGS) multi-GNSS experiment (MGEX) network. In order to ensure the reliability of time-frequency transfer, the stations of UTC (Coordinated Universal Time) laboratories were preferred in our research. The sampling interval of the observations was 30 s. These stations were all equipped with high-precision atomic clocks. With the BRUX station as the reference station, four time-frequency links ranging from 454.6 km to 5591.2 km were established. Figure 1 shows the distribution of the selected MGEX stations, the information of which is listed in Table 2.

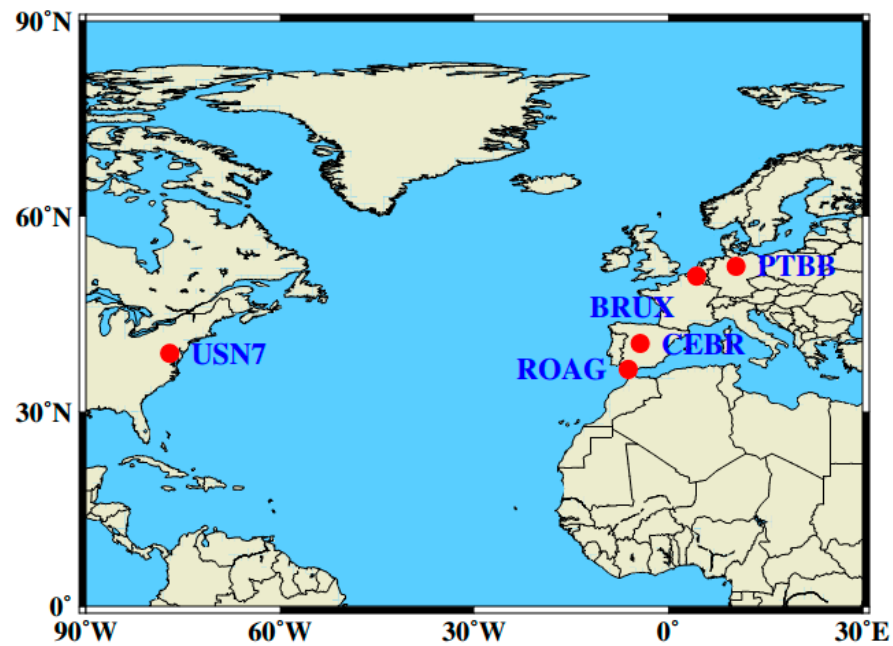


Figure 1. Geographic distribution of the selected stations.

Table 2. List of selected MGEX stations.

Stations	Receiver	Antenna	Clock	Country	Distance
BRUX	SEPT POLARX5TR	JAVRINGANT_DM	UTC (ORB)	Belgium	/
CEBR	SEPT POLARX5TR	SEPCHOKE_B3E6	H-MASER	Spain	1331.6 km
PTBB	SEPT POLARX5TR	LEIAR25.R4	UTC (PTB)	Germany	454.6 km
ROAG	SEPT POLARX5TR	LEIAR25.R4	UTC (ROA)	Spain	1796.3 km
USN7	SEPT POLARX5TR	TPSCR.G5	UTC (USNO)	America	5991.2 km

The code and phase observation noises were set to 0.3 m and 3.0 mm, respectively, and elevation-dependent weighting for the observations was applied. Since the receiver phase center offset (PCO) and phase center variation (PCV) corrections for Galileo were not available, we used the GPS signal corrections for Galileo signals. Such a strategy has been used effectively by various authors [29,30]. In addition, for the E5b, E5, and E6 observables, receiver PCO and PCV corrections for the GPS L2 frequency were used. Since different observations were used in the same satellite clock estimation, there were IFCBs in the E5b, E5 and E6 observations [31]. Relevant research shows that the consistency of Galileo multifrequency time-dependent UCDs can be ensured; thus, IFCBs in the Galileo system can be neglected [30]. The detailed processing strategies are summarized in Table 3.

Table 3. Detailed processing strategies.

Items	Strategies
Solutions	DF/TF/QF/FF1/FF2/FF2/FF3/FF4/UC PPP models
Observations	E1/E5a/E5b/E5/E6 observations
Elevation cutoff	7°
Orbits and clock	GBM, WUM and GRG precise products
Satellite DCB	CAS BSX products [32], E1I : $-\beta_{12} \cdot DCB_{12}$, E5a : $\alpha_{12} \cdot DCB_{12}$, E5b : $\alpha_{12} \cdot DCB_{12} - DCB_{23}$, E5 : $\alpha_{12} \cdot DCB_{12} - DCB_{24}$, E6 : $\alpha_{12} \cdot DCB_{12} - DCB_{25}$
Earth rotation	Corrected [33]

Table 3. Cont.

Items	Strategies
Relativistic effect	Corrected [34]
Phase windup effect	Corrected [35]
Tide effect	Corrected [36]
PCO/PCV	IGS14.atx
Station coordinates	Estimated as constants
Receiver clock	Estimated as white noises (10^4 m ² /s) UC: Estimated as random walk process
Ionospheric delay	DF/TF/QF/FF1/FF2/FF3/FF4: Eliminated first-order by <i>IF</i> combinations Dry component: GPT add Saastamoinen model [37,38]
Tropospheric delay	Wet component: Estimated as random walk part (10^{-8} m ² /s), GMF mapping function [39]
Ambiguities	Estimated as constant, float solution

3. Results

First, we evaluated the number of visible satellites, time dilution of precision (TDOP) and multipath noises of BRUX, CEBR, PTBB, ROAG and USN7 stations with Galileo satellites. Then, the positioning performances and time-frequency transfer stabilities of four models (DF, TF, QF and FF1) composed of dual-frequency, triple-frequency, quad-frequency, and five-frequency observations were compared by PPP solution; the positioning accuracies, *IFB* parameters and time-frequency transfer stabilities of the five-frequency observation models (FF1, FF2, FF2, FF3, FF4 and UC) were also evaluated. Finally, we used different AC precise products to compare and evaluate the performances of different PPP models. It should be noted that the positioning performance was assessed with respect to the coordinates from the IGS SNX file, and the principle of convergence was that the three-dimensional (3D) bias of twenty successive epochs is better than 10.0 cm; in addition, the 3D root mean square (RMS) values after convergence were counted. The modified Allan deviation (MADEV) was used as the stability index of time-frequency transfer.

3.1. Number of Visible Satellites, TDOP and Multipath Combination Noise Analysis

Until July 2020, the Galileo system had twenty-four valid satellites in orbit, including four in-orbit validation (IOV) satellites and twenty fully operational capability (FOC) satellites. The distribution of the average number of visible satellites and average position dilution of precision (PDOP) values for the GPS and Galileo constellations with a cutoff elevation of 5.0 degrees with a $1^\circ \times 1^\circ$ grid on days of year (DOYs) 190 to 196 in 2020 are shown in Figure 2.

As shown in Figure 2, the number of visible satellites and the PDOP value of the GPS and Galileo constellations are symmetrically distributed with the equator, which shows a strong correlation with the dimension, and the positioning performance is better near the equator; the average number of visible satellites of Galileo ranges from 7.0 to 10.0, and the average PDOP value of Galileo ranges from 1.6 to 2.1. By comparison, the average number of visible satellites of Galileo is slightly less than that of GPS, and the PDOP value of Galileo is slightly larger than that of GPS.

Figure 3 presents the number of visible satellites and TDOP values of the five stations. When the cutoff satellite elevation is 7 degrees, the average numbers of visible satellites at stations BRUX, CEBR, PTBB, ROAG and USN7 are 7.08, 6.6, 7.05, 6.68 and 8.85, respectively. Among them, the number of visible satellites with gross error removed at some moments of CEBR and USN7 stations are less than 4.0, which cannot be a PPP solution. It can be observed from the right figure that the TDOP values of the five stations all have some noise phenomenon, which will affect the accuracy of the time-frequency transfer of this epoch. The average TDOPs of the BRUX, CEBR, PTBB, ROAG and USN7 stations are 1.12, 1.29, 1.14, 1.26 and 1.26, respectively.

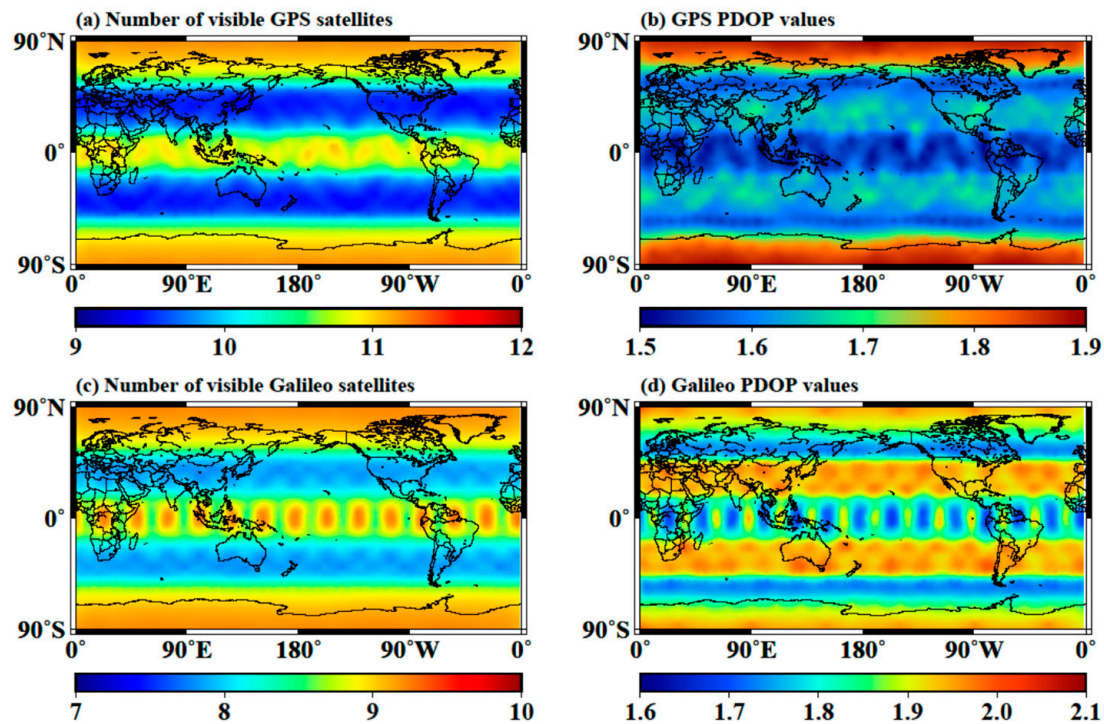


Figure 2. Distribution of number of visible satellites and position dilution of precision (PDOP) value for GPS and Galileo constellation on days of year (DOYs) 190 to 196 in 2020. (a) Number of visible GPS satellites; (b) GPS PDOP values; (c) number of visible Galileo satellites; and (d) Galileo PDOP values.

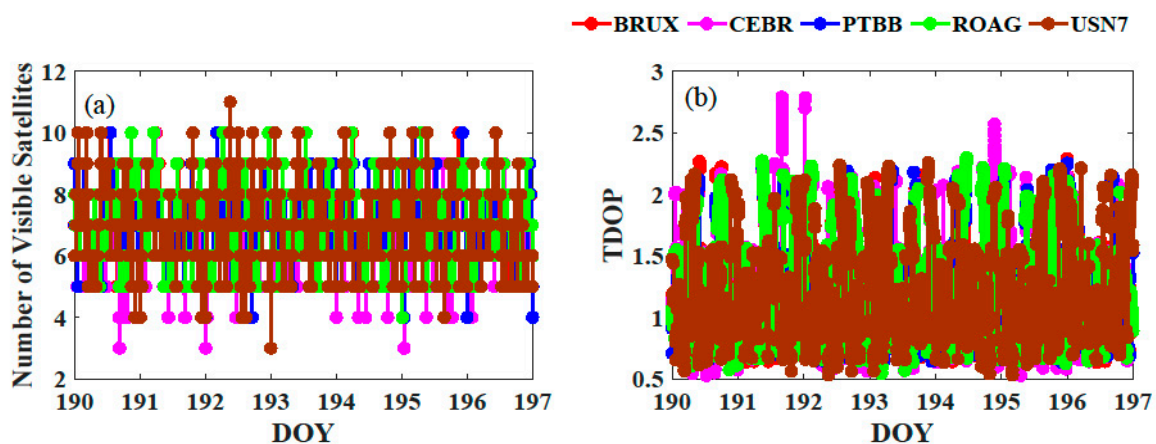


Figure 3. Number of visible satellites and time dilution of precision (TDOP) values at BRUX and PTBB for Galileo on DOYs 190 to 196 in 2020. (a) Number of visible satellites; and (b) TDOP values.

As shown in Figure 4, the multipath combination noise of each frequency is within ± 2.0 m, among which the multipath combination noise of the E1 frequency is the largest and that of the E5 frequency is the smallest. When the cutoff elevation is 7 degrees, the BRUX station E1, E5a, E6, E5 and E5b multipath combination noise RMS values are 0.224 m, 0.166 m, 0.190 m, 0.116 m and 0.198 m, respectively; the CEBR station E1, E5a, E6, E5 and E5b multipath combination noise RMS values are 0.319 m, 0.305 m, 0.350 m, 0.144 m and 0.312 m, respectively; the PTBB station E1, E5a, E6, E5 and E5b multipath combination noise RMS values are 0.311 m, 0.209 m, 0.243 m, 0.161 m and 0.247 m, respectively; the ROAG station E1, E5a, E6, E5 and E5b multipath combination noise RMS values are 0.166 m, 0.126 m, 0.148 m, 0.083 m, and 0.149 m, respectively; and the USN7 station E1, E5a, E6, E5 and E5b multipath combination noise RMS values are 0.378 m, 0.307 m, 0.355 m, 0.130 m

and 0.331 m, respectively. It is obvious that the multipath combination noise of the CEBR station and USN7 station is the largest and that of the ROAG station is the smallest.

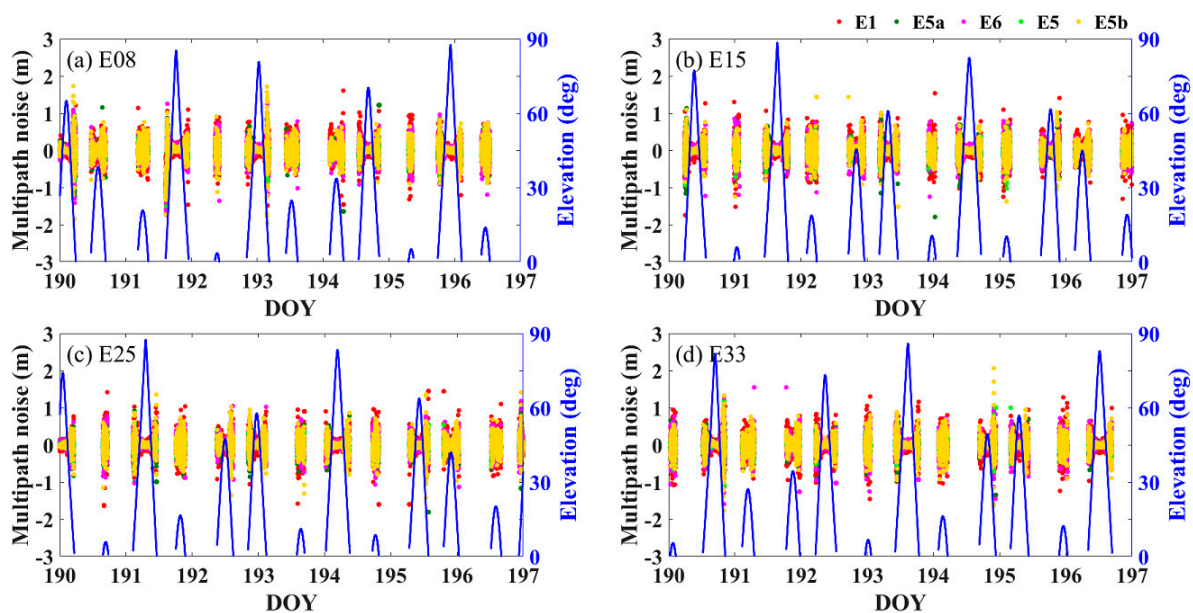


Figure 4. Galileo multipath combination noise sequence and elevation at frequencies E1, E5a, E6, E5 and E5b at BRUX station on DOYs 190 to 196 in 2020. (a) E08 satellite; (b) E15 satellite; (c) E25 satellite; and (d) E33 satellite.

3.2. Performance of the DF, TF, QF and FF1 PPP Models

As shown in Figure 5, the positioning RMS values and convergence times of the DF, TF, QF and FF1 PPP models are close to each other. With the increasing of the frequency, the positioning performance has no obvious improvement, and some stations have even weakened. Among them, the PPP performance of station USN7 is obviously weaker than that of the other stations, especially the E and N components, which have large changes in the TF PPP model. The convergence times of the BRUX, CEBR and ROAG stations are less than 15.0 min, and those of the PTBB and USN7 stations are approximately 25.0 min. According to the statistics, the average 3D RMS values of the DF, TF, QF and FF1 PPP models are 1.88 cm, 1.95 cm, 1.85 cm, and 1.78 cm, respectively; the average convergence times are 16.6 min, 16.6 min, 16.7 min and 17.3 min, respectively.

The clock offset sequences of the DF, TF, QF and FF1 PPP models are shown in Figure 6. Due to the influence of *IFB* parameters, the clock offsets of the various PPP models show a certain deviation, and the deviations of the TF and QF models are minimal. The RMS deviations between the TF, QF, FF1 and DF PPP models of the BRUX-CEBR link are 0.30 ns, 0.06 ns and 1.46 ns, respectively; the RMS deviations between the TF, QF, FF1 and DF PPP models of the BRUX-PTBB link are 0.89 ns, 0.93 ns and 0.26 ns, respectively; the RMS deviations between the TF, QF, FF1 and DF PPP models of the BRUX-ROAG link are 1.66 ns, 1.50 ns and 0.21 ns, respectively; and the RMS deviations between the TF, QF, FF1 and DF PPP models of the BRUX-USN7 link are 0.49 ns, 0.50 ns and 0.99 ns, respectively.

As shown in Table 4, the average values among the four time-frequency links in each model are completely consistent, and the RMS values have only slight deviations, which indicates that the multifrequency stability is not significantly improved compared with the dual-frequency stability. The RMS value of the inter-epoch difference of the BRUX-CEBR link is approximately 10.5 ps, and those of the other three time-frequency links are less than 8.2 ps, which indicates that the frequency stability of the BRUX-CEBR link is worse. In addition, it is noted that the hydrogen atomic clock attached to the BRUX-CEBR link has obvious clock drift, which is related to the performance of the CEBR station atomic clock.

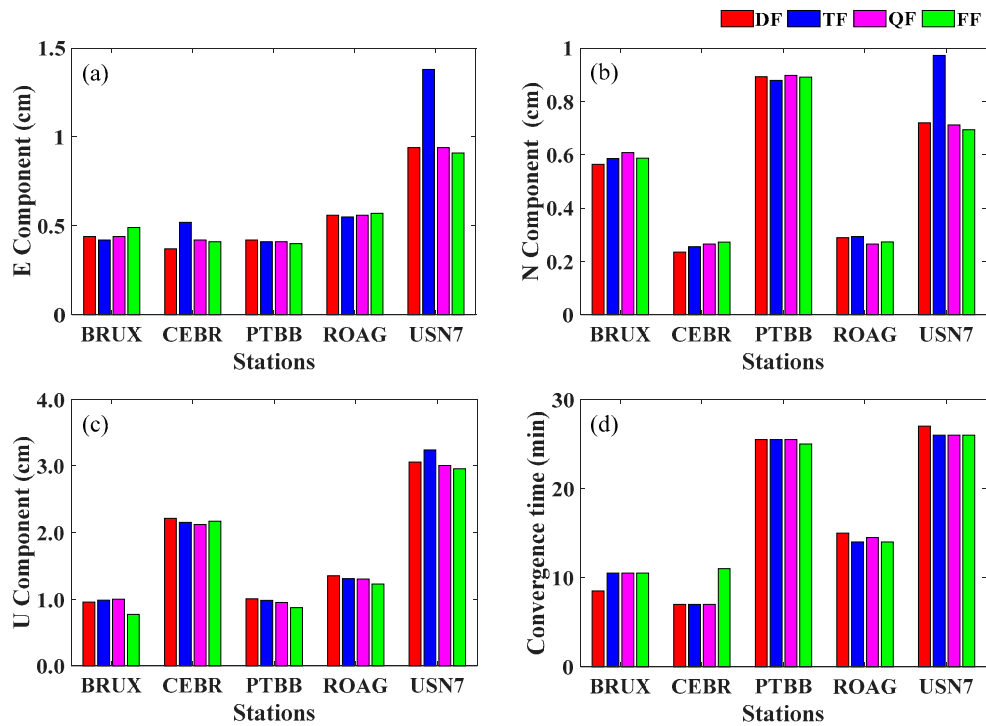


Figure 5. Positioning performance of BRUX, CEBR, PTBB, ROAG and USN7 stations for the DF, TF, QF and FF1 PPP models on DOYs 190 to 196 in 2020. (a) E component RMS value; (b) N component RMS value; (c) U component RMS value; and (d) convergence time.

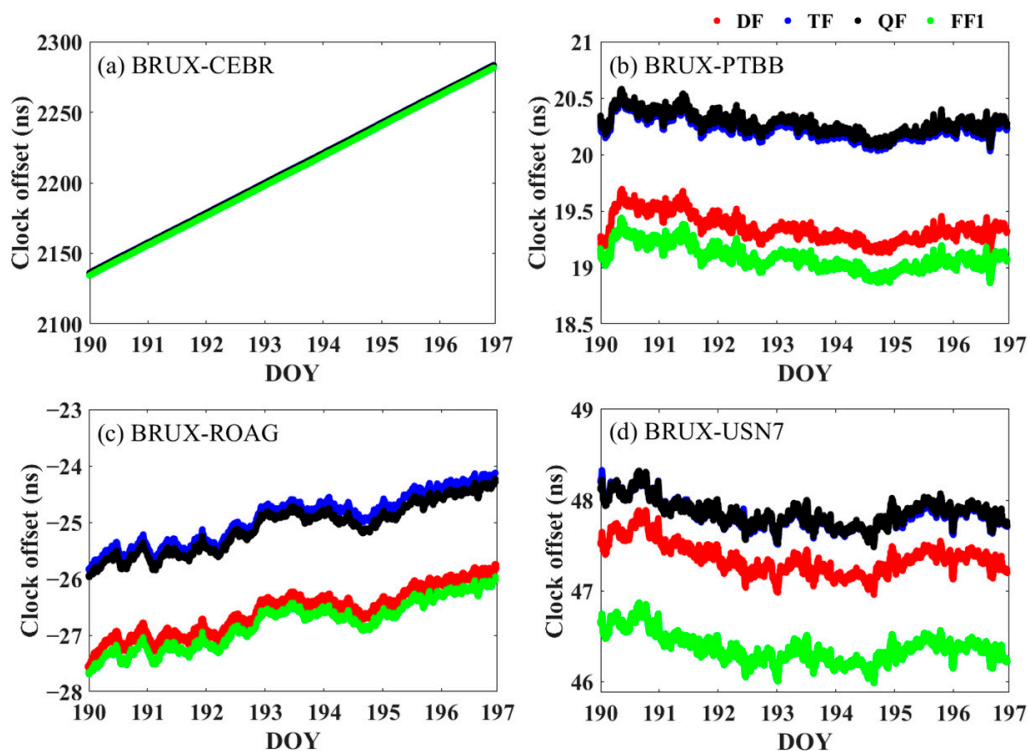


Figure 6. Clock offset sequence at four time-frequency links for the DF, TF, QF and FF1 PPP models on DOYs 190 to 196 in 2020. (a) BRUX-CEBR time-frequency link; (b) BRUX-PTBB time-frequency link; (c) BRUX-ROAG time-frequency link; and (d) BRUX-USN7 time-frequency link.

Table 4. Clock offset epoch difference results of average (AVG) and root mean square (RMS) at four time-frequency links for the DF, TF, QF and FF1 PPP models on DOYs 190 to 196 in 2020 (ps).

Items	Links	DF	TF	QF	FF1
AVG	BRUX-CEBR	7.38	7.38	7.38	7.38
	BRUX-PTBB	0.01	0.01	0.01	0.01
	BRUX-ROAG	0.08	0.08	0.08	0.08
	BRUX-USN7	−0.01	−0.01	−0.01	−0.01
RMS	BRUX-CEBR	10.54	10.44	10.50	10.49
	BRUX-PTBB	7.02	6.88	6.97	6.87
	BRUX-ROAG	7.22	7.09	7.17	7.14
	BRUX-USN7	7.98	7.88	8.02	8.14

Figure 7 presents a comparison of the frequency stabilities for the DF, TF, QF and FF1 PPP models, which are generally identical for different solutions at the four time-frequency links. The frequency stability of the BRUX-PTBB link reaches the 10^{-16} level in 60,000 s and 5.31×10^{-16} in 120,000 s, the BRUX-USN7 link reaches 9.25×10^{-16} in 120,000 s, and those of the other two links are also close to the 10^{-16} level in 120,000 s. The average frequency stabilities at 120,000 s for the four time-frequency links surpass 1.23×10^{-15} for the DF PPP model, 1.15×10^{-15} for the TF PPP model, 1.23×10^{-15} for the QF PPP model and 1.23×10^{-15} for the FF1 PPP model.

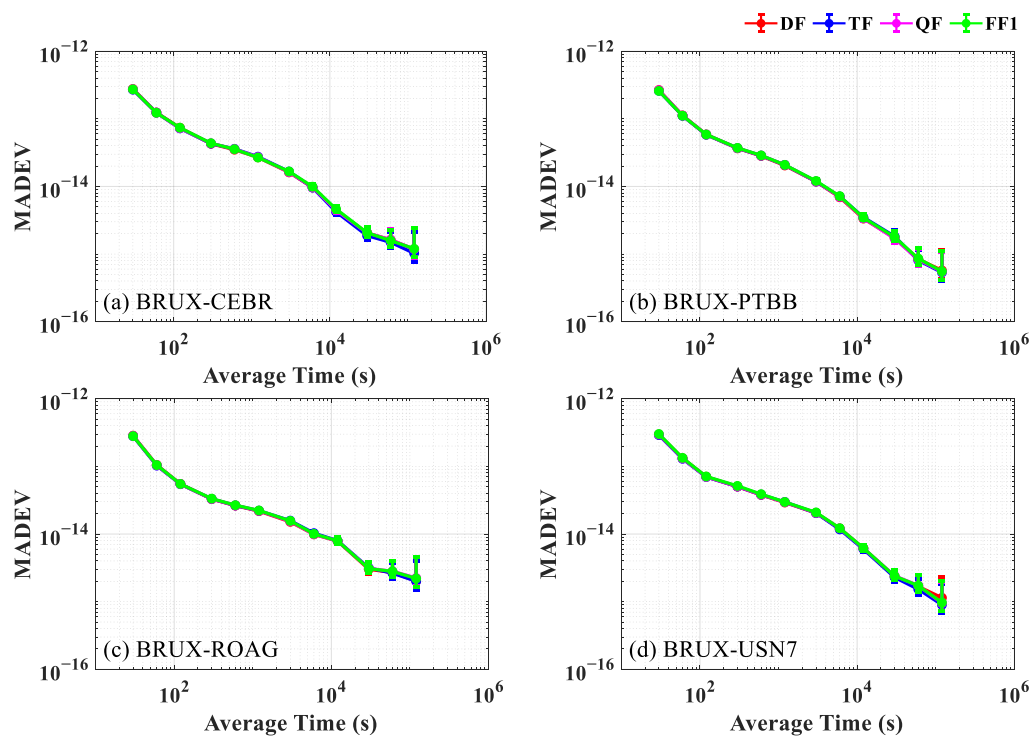


Figure 7. MADEV at four time-frequency links for the DF, TF, QF and FF1 PPP solutions on DOYs 190 to 196 in 2020. (a) BRUX-CEBR time-frequency link; (b) BRUX-PTBB time-frequency link; (c) BRUX-ROAG time-frequency link; and (d) BRUX-USN7 time-frequency link.

3.3. Performance of the FF1, FF2, FF3, FF4 and UC PPP Models

Figure 8 presents the positioning performances of the FF1, FF2, FF3, FF4 and UC PPP models. The positioning performances of several Galileo five-frequency PPP models are basically the same, but USN7 station E and U component RMS values by UC PPP are slightly worse. According to the statistics, the average 3D RMS values of the DF, TF, QF and FF1 PPP models are 1.78 cm, 1.85 cm, 1.82 cm, 1.74 cm, and 1.73 cm, respectively; and

the average convergence times are 17.3 min, 16.6 min, 16.6 min, 17.3 min, and 17.4 min, respectively.

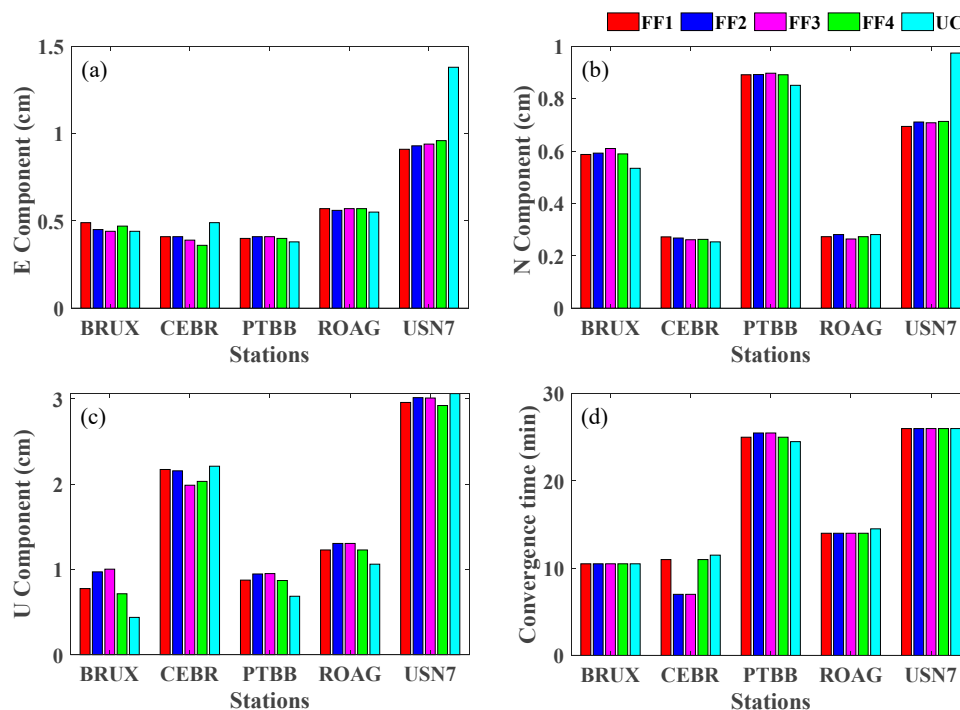


Figure 8. Positioning performance of the BRUX, CEBR, PTBB, ROAG and USN7 stations by the FF1, FF2, FF3, FF4 and UC PPP solutions on DOYs 190 to 196 in 2020. (a) E Component RMS value; (b) N component RMS value; (c) U component RMS value; and (d) convergence time.

Figure 9 presents the clock offsets of five-frequency PPP models, and each clock offset sequence has the same trend, which proves the correctness of the algorithm. In addition, there are some deviations among the clock offsets, among which the FF1 and FF2 PPP models and the FF4 and UC PPP models have minimum deviations. Based on the clock offset of the FF1 model, the RMS values of FF2, FF3, FF4 and UC compared with FF1 in the BRUX-CEBR link are 1.56 ns, 1.86 ns, 1.49 ns and 1.44 ns, respectively; the RMS values of the FF2, FF3, FF4 and UC PPP models compared with the FF1 PPP model in the BRUX-PTBB link are 1.17 ns, 1.15 ns, 0.25 ns and 0.25 ns, respectively; the RMS values of FF2, FF3, FF4 and UC compared with FF1 in the BRUX-ROAG link are 1.71 ns, 1.87 ns, 1.49 ns and 0.23 ns, respectively; and the RMS values of FF2, FF3, FF4 and UC compared with FF1 in the BRUX-ROAG link are 1.51 ns, 1.01 ns and 1.01 ns, respectively.

As shown in Table 5, the average RMS values of the BRUX-CEBR, BRUX-PTBB, BRUX-ROAG and BRUX-USN7 time-frequency links are 10.48 ps, 6.90 ps, 7.11 ps and 8.09 ps, respectively; and the average RMS values of the FF1, FF2, FF3, FF4 and UC models are 8.16 ps, 8.16 ps, 8.17 ps, 8.08 ps and 8.16 ps, respectively. It is worth noting that although in the UC model, one needs to estimate the ionospheric delay since the receiver clock bias is easily affected by the unmodeled ionospheric delay, the AVG and RMS of the UC model are still close to those of the *IF* PPP models.

Figure 10 presents comparisons of the MADEVs for the FF1, FF2, FF3, FF4 and UC PPP models. The MADEVs of the PPP models with different five-frequency combinations are basically the same. The average frequency stabilities at 120,000 s for four time-frequency links surpassed 1.23×10^{-15} for the FF1 PPP model, 1.22×10^{-15} for the FF2 PPP model, 1.20×10^{-15} for the FF3 PPP model and 1.24×10^{-15} for the UC PPP model.

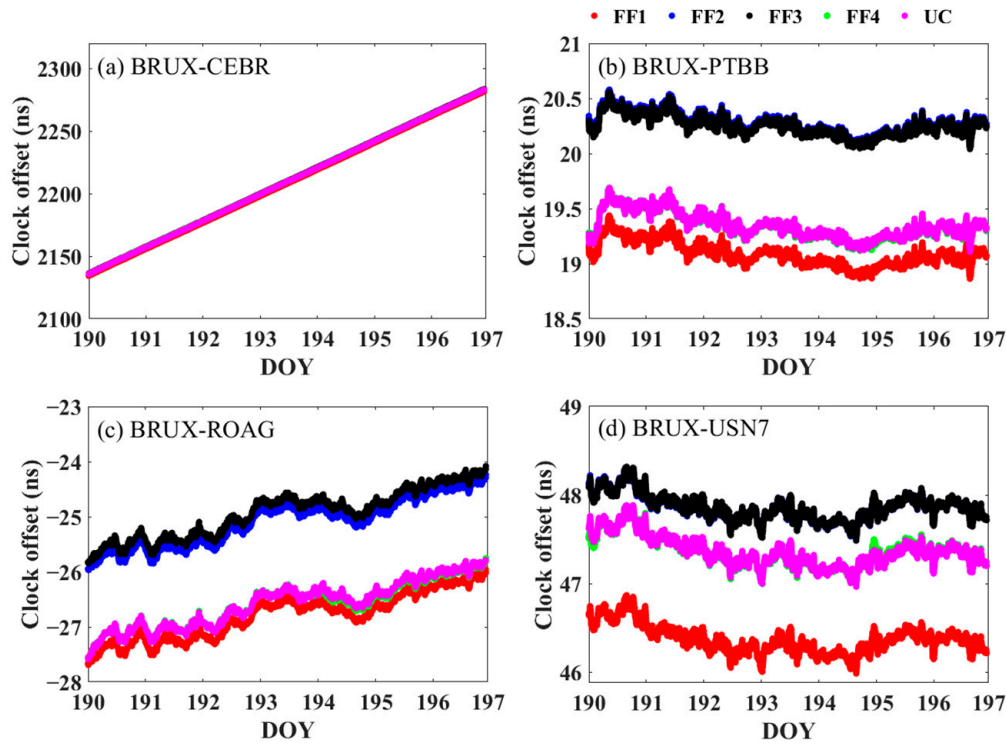


Figure 9. Clock offset sequences at four time-frequency links for the FF1, FF2, FF3, FF4 and UC PPP solutions on DOYs 190 to 196 in 2020. (a) BRUX-CEBR time-frequency link; (b) BRUX-PTBB time-frequency link; (c) BRUX-ROAG time-frequency link; and (d) BRUX-USN7 time-frequency link.

Table 5. Clock offset epoch difference results at four time-frequency links for the FF1, FF2, FF3, FF4 and UC PPP models on DOYs 190 to 196 in 2020 (ps).

Item	Links	FF1	FF2	FF3	FF4	UC
AVG	BRUX-CEBR	7.38	7.38	7.40	7.38	7.38
	BRUX-PTBB	0.01	0.01	0.01	−0.01	0.01
	BRUX-ROAG	0.08	0.08	0.08	0.08	0.08
	BRUX-USN7	−0.01	−0.01	−0.01	−0.01	−0.01
RMS	BRUX-CEBR	10.49	10.51	10.53	10.40	10.46
	BRUX-PTBB	6.87	6.92	6.95	6.84	6.92
	BRUX-ROAG	7.14	7.15	7.16	7.09	7.03
	BRUX-USN7	8.14	8.04	8.04	8.00	8.23

As shown in Figure 11, the *IFB* sequences are basically stable, and the *IFB* values of the FF4 model are the largest. The average RMS values of IFB_{IF13} , IFB_{IF14} , and IFB_{IF15} in the FF4 PPP model are 7.8 ns, 4.1 ns, and 9.9 ns, respectively; and the average STD values are 0.04 ns, 0.03 ns, and 0.15 ns, respectively. The average RMS values of IFB_{UC3} , IFB_{UC4} , and IFB_{UC5} in the UC PPP model are 5.49 ns, 3.09 ns, and 5.15 ns, respectively, and the corresponding average STD values are 0.03 ns, 0.02 ns, and 0.04 ns, respectively. As mentioned, the IFB_{IF15} STD value of the FF4 PPP model is the largest, leading to the receiver clock bias, and IFB_{IF15} cannot be accurately separated, which will affect the time-frequency transfer performance.

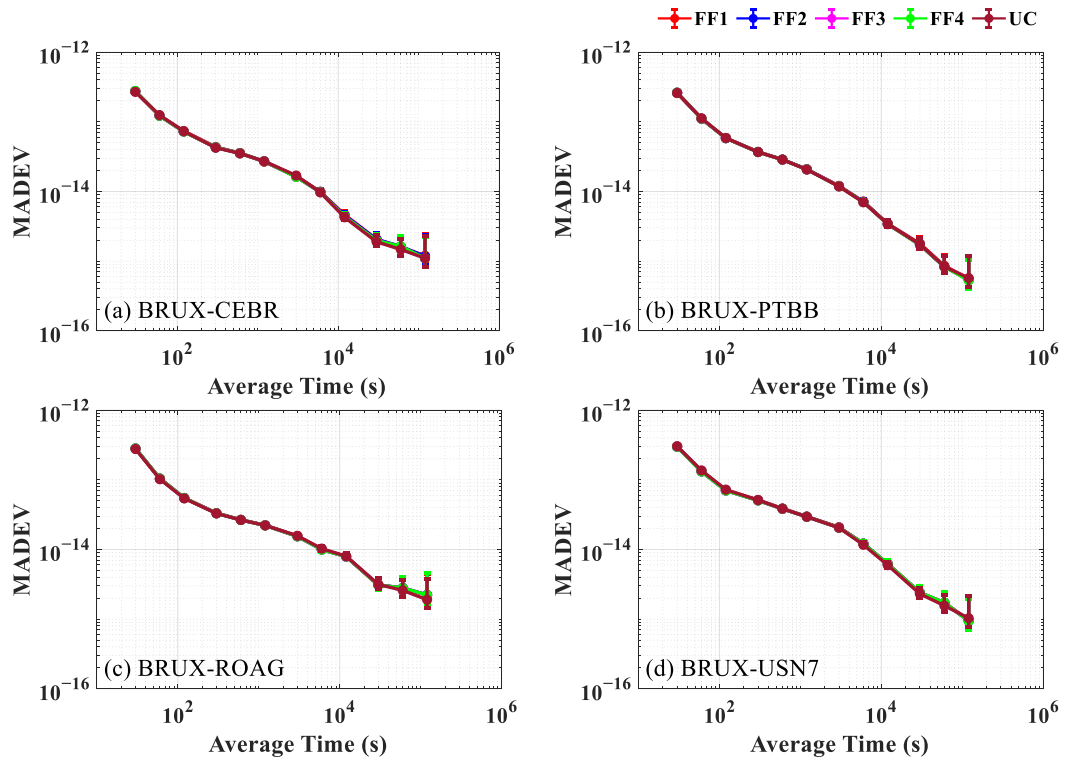


Figure 10. MADEV at four time-frequency links for the FF1, FF2, FF3, FF4 and UC PPP solutions on DOYs 190 to 196 in 2020. (a) BRUX-CEBR time-frequency link; (b) BRUX-PTBB time-frequency link; (c) BRUX-ROAG time-frequency link; and (d) BRUX-USN7 time-frequency link.

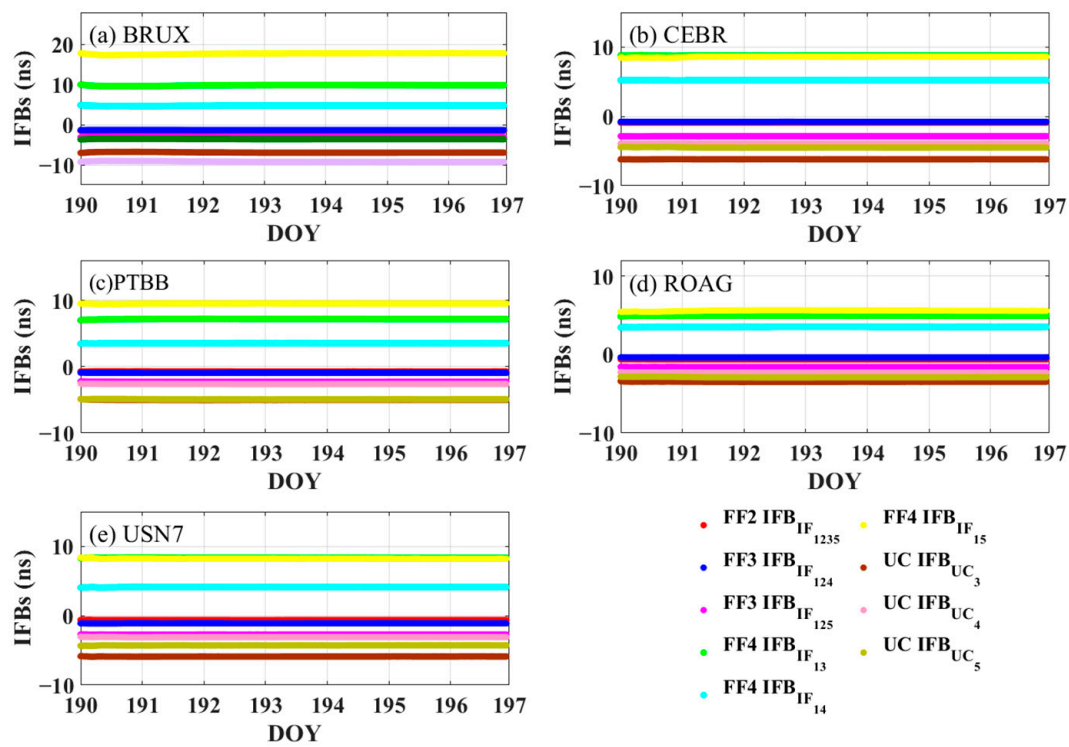


Figure 11. IFB sequences at five stations for the FF2, FF3, FF4 and UC PPP models on DOYs 190 to 196 in 2020. (a) BRUX station; (b) CEBR station; (c) PTBB station; (d) ROAG station; and (e) USN7 station.

3.4. PPP Performance by Using Different AC Products

To further evaluate the performance of Galileo's five-frequency PPP model, the WUM and GRG precise ephemeris and clock products are used for experiments. It should be noted that the GRG clock product has absorbed the UPD of the satellite side, and the GBM and WUM clock products have absorbed the UCD of the satellite side, with some differences. The average convergence times and average 3D RMS values at five stations of the DF, TF, QF, FF1, FF2, FF3, FF4 and UC PPP models are shown in Figure 12.

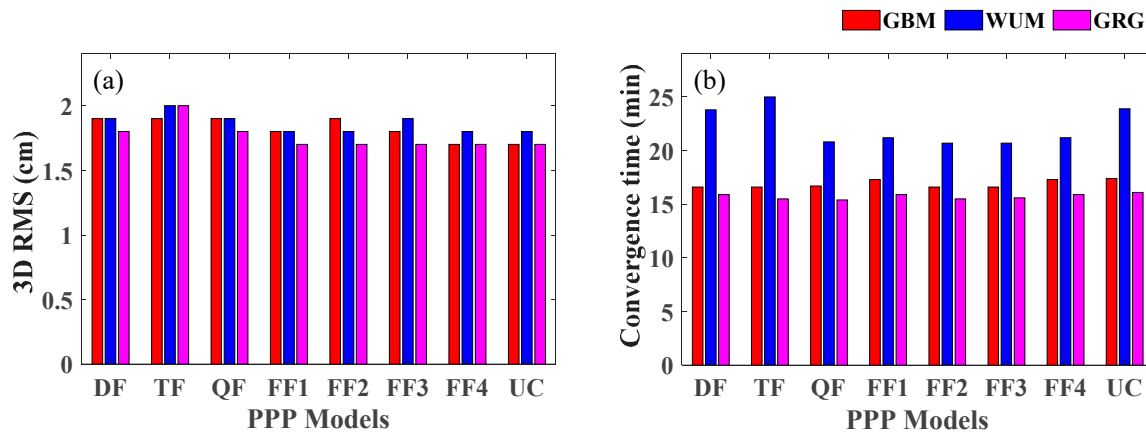


Figure 12. Average 3D RMS values and average convergence times by using the GBM, WUM and GRG precise product PPP solutions on DOYs 190 to 196 in 2020. (a) 3D RMS value; (b) convergence time.

The convergence times of the WUM product are significantly longer than those of the GBM and GRG products, and the average convergence time of the GRG product is the shortest. Compared with the dual-frequency PPP model, the multifrequency PPP model does not significantly improve the convergence speed. The average convergence times using the GBM, WUM and GRG products are 16.8 min, 22.2 min, and 15.7 min, respectively. Compared with the results using the GRM and WUM products, the average convergence speed obtained using the GRG product is increased by 6.8% and 29.1%, respectively. The average 3D RMS values obtained using the GBM, WUM and GRG products are 1.82 cm, 1.85 cm, and 1.77 cm, respectively. Compared with the results using the GRM and WUM products, the positioning accuracy achieved using the GRG product is improved by 2.7% and 4.3%, respectively.

Limited by space, Figure 13 only shows the clock offsets of the FF1 PPP model by using the GBM, WUM and GRG precise products. The clock offsets of the BRUX-CEBR, BRUX-PTBB and BRUX-ROAG time-frequency links are completely consistent, and there is only a small constant deviation term. Although the BRUX-USN7 clock offset trend is consistent, the deviation is slightly larger, which may be related to the quality of the observations of USN7. According to statistics, the deviations of the BRUX-CEBR link using GBM products compared with WUM and GRG products are 0.02 ns and 0.03 ns, respectively; the deviations of the BRUX-PTBB link using GBM products compared with WUM and GRG products are all 0.01 ns; the deviations of the BRUX-ROAG link using GBM products compared with WUM and GRG products are all 0.03 ns; and the deviations of the BRUX-USN7 link using GBM product compared with WUM and GRG products are 0.08 ns and 0.09 ns, respectively.

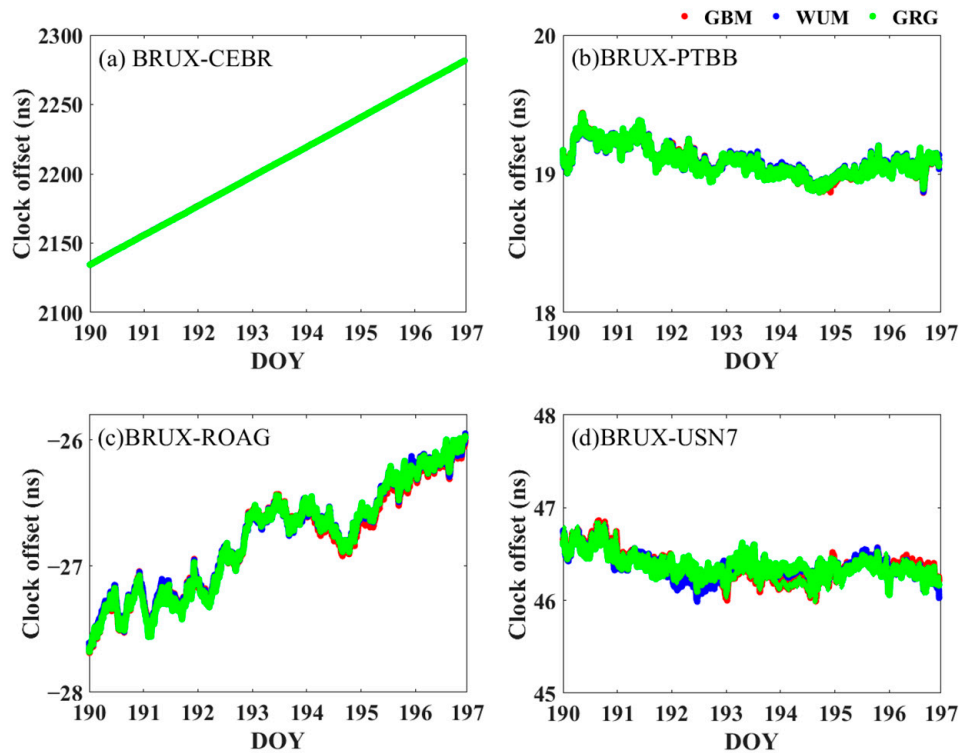


Figure 13. Clock offset sequences of the GBM, WUM and GRG products in the PPP FF1 model. (a) BRUX-CEBR time-frequency link; (b) BRUX-PTBB time-frequency link; (c) BRUX-ROAG time-frequency link; and (d) BRUX-USN7 time-frequency link.

Table 6 shows the RMS values of the epoch difference by using WUM and GRG precision products for the PPP solution. The average RMS values of the BRUX-CEBR, BRUX-PTBB, BRUX-ROAG and BRUX-USN7 time-frequency links with the WUM product are 10.54 ps, 7.01 ps, 7.14 ps, and 8.24 ps, respectively, while those of the BRUX-CEBR, BRUX-PTBB, BRUX-ROAG and BRUX-USN7 time-frequency links with the GRG product are 10.57 ps, 7.02 ps, 7.22 ps, and 8.18 ps, respectively, which is consistent with the solution results obtained using the precise GBM product.

Table 6. Clock offset epoch difference RMS at four time-frequency links by the WUM and GRG product PPP solutions on DOYs 190 to 196 in 2020 (ps).

Products	Links	DF	TF	QF	FF1	FF2	FF3	FF4	UC
WUM	BRUX-CEBR	10.62	10.59	10.55	10.49	10.49	10.52	10.52	10.55
	BRUX-PTBB	7.1	7.02	7.04	6.96	7.02	7.02	6.95	6.98
	BRUX-ROAG	7.27	7.11	7.16	7.12	7.16	7.16	7.04	7.13
	BRUX-USN7	8.08	9.02	8.05	8.15	8.11	8.08	8.34	8.06
GRG	BRUX-CEBR	10.65	10.53	10.54	10.51	10.55	10.51	10.76	10.52
	BRUX-PTBB	7.08	7.01	7.00	6.92	6.99	6.91	7.31	6.96
	BRUX-ROAG	7.30	7.24	7.21	7.17	7.20	7.16	7.27	7.19
	BRUX-USN7	8.07	8.11	8.00	8.12	8.04	8.11	8.92	8.03

As shown in Figure 14, the frequency stabilities of the BRUX-CEBR, BRUX-PTBB and BRUX-USN7 links can reach the 10^{-16} level, and the frequency stability of the BRUX-USN7 link using the GRG product is the most significantly improved compared to those using WUM and GRG products, which may be related to the observation quality of USN7 and the absorption of satellite UPD by GRG clock products. The average frequency stabilities over four links using GBM, WUM and GRG products in 120,000 s are 1.18×10^{-15} , 1.13×10^{-15} and 1.06×10^{-15} , respectively. Using WUM products, the average frequency stabilities of the DF, TF, QF, FF1, FF2, FF3, FF4 and UC PPP models are 1.12×10^{-15} , 1.13×10^{-15} ,

1.13×10^{-15} , 1.15×10^{-15} , 1.12×10^{-15} , 1.11×10^{-15} , 1.13×10^{-15} , and 1.15×10^{-15} , respectively, while using GRG products, the corresponding average frequency stabilities are 1.05×10^{-15} , 1.07×10^{-15} , 1.05×10^{-15} , 1.06×10^{-15} , 1.05×10^{-15} , 1.03×10^{-15} , 1.05×10^{-15} and 1.10×10^{-15} , respectively. All these results demonstrate that the frequency stability using the GRG product is better than those using WUM and GBM products at 120,000 s. It can also be found that compared with the DF model, the multifrequency model's frequency stabilities are not significantly improved, which may be limited by the additional estimation of *IFB* parameters and the accuracy of multifrequency *DCB* products [40].

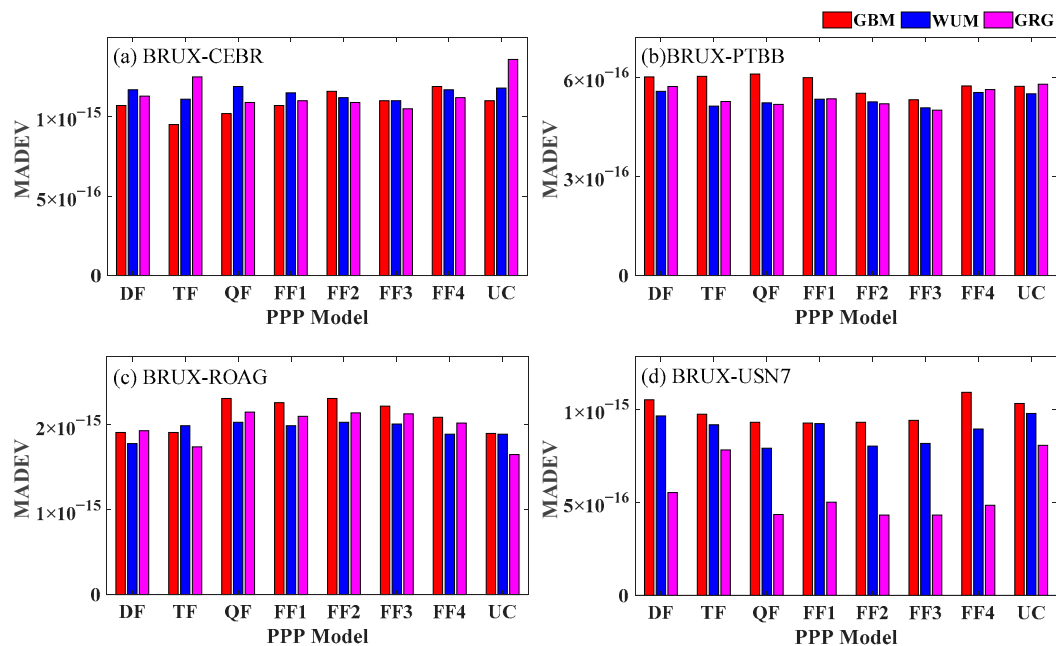


Figure 14. MADEV of the PPP solution by using GBM, WUM and GRG precision products at 120,000 s. (a) BRUX-CEBR time-frequency link; (b) BRUX-PTBB time-frequency link; (c) BRUX-ROAG time-frequency link; and (d) BRUX-USN7 time-frequency link.

To deeply analyze the frequency transfer stability of the BRUX-USN7 link, Figure 15 shows the frequency stability of the BRUX-USN7 link by using different ACs precision products. The frequency stability obtained using the GBM, WUM and GRG products before 30,000 s is completely consistent, but the frequency stability achieved using GRG products between 30,000 s and 120,000 s is significantly improved compared with using the GBM and WUM products. Compared with GBM and WUM, the stability obtained using GRG products is increased by 33.83% and 40.62% on average, respectively, and with the increase in time, the improvement range of stability gradually increases, which indicates that using GRG products has certain advantages over using GBM and WUM products in long-term frequency stability.

4. Discussion

With GNSS interoperability and support for multiple signal frequencies, the era of multi frequency and multi system PNT services has come. Compared with the traditional DF model, the multi frequency combination will be able to look for smaller noise coefficients, improve the reliability of the system, and help to achieve fast fixed ambiguity. At the same time, it will also face the challenge of *IFB* and *IFCB* processing in multi frequency signals. This research is a new exploration of Galileo five frequency signal PPP models, which systematically realizes the comparison and evaluation of Galileo TF, DT, FF, and DF models in terms of precision positioning and time-frequency transfer performance. Although the noise amplification factor of some multi frequency combination models decreases, the

estimated *IFB* parameters are increased with the increase in the component observation equation. The precise separation of *IFBs* from clock bias and ambiguity parameters, the setting of multi frequency observation noise and the accuracy of multi frequency *DCB* products also affect the performance of five frequency PPP models. With the improvement of multi frequency *DCB* products, combined with the advantages of multi-frequency signals in redundancy, low noise, and long wavelength, it is reasonable to consider that Galileo five frequency signal will be more widely used in the future. In subsequent research, we will determine the noise of multi frequency observations and explore the performance of multi frequency signal in terms of ambiguity resolution.

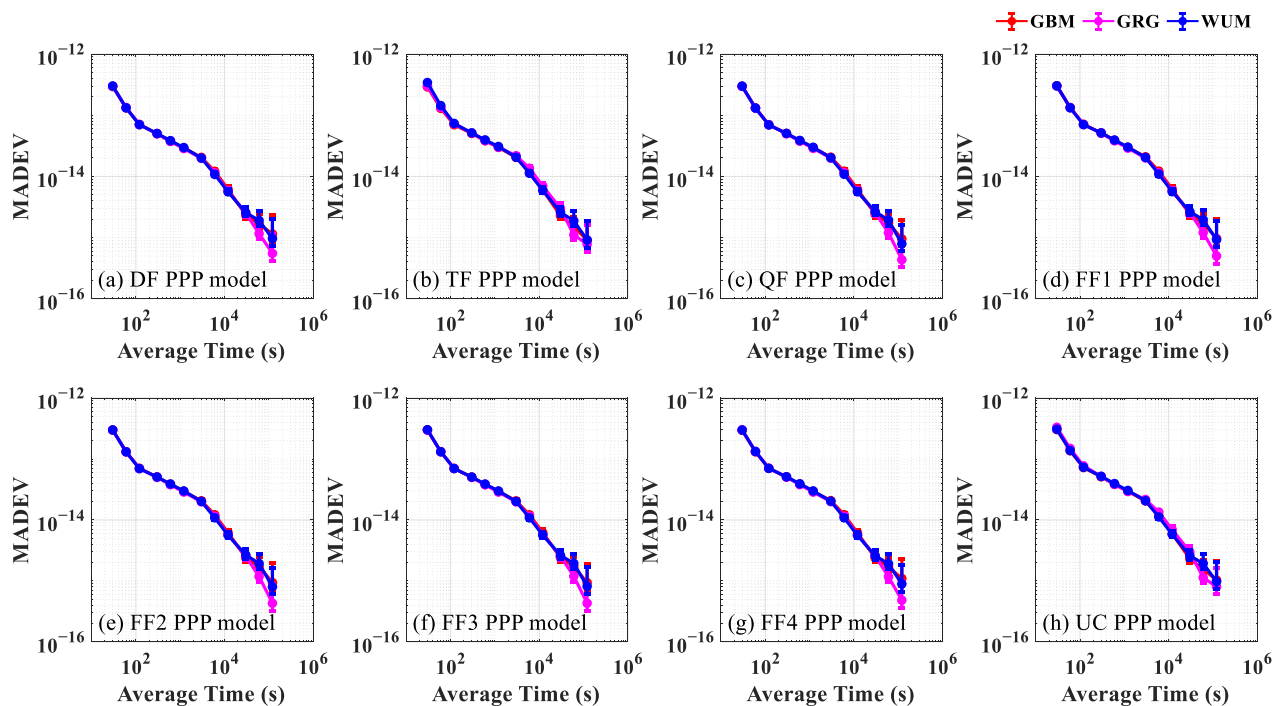


Figure 15. MADEV at the BRUX-USN7 time-frequency link of the PPP solution by using GBM, WUM and GRG precision products on DOYs 190 to 196 in 2020. (a) DF PPP model; (b) TF PPP model; (c) QF PPP model; (d) FF1 PPP model; and (e) FF2 PPP model; (f) FF3 PPP model; (g) FF4 PPP model; (h) UC PPP model.

It should be noted that in order to meet the performance of time-frequency transfer, we need to select the stations that support the Galileo five-frequency observation signals and are connected the external high-precision hydrogen atomic clocks. After eliminating stations with poor data quality and choosing the preferred stations of UTC laboratories, there are only a few proper suitable stations in the MGEX network. At the same time, scientists are more concerned about the index of the daily stability, which can basically reflect the best performance of the atomic clocks. The time-frequency links selected in this study are very representative, and the length of the observations can meet the requirements of short-term stability and long-term stability. In addition, our study evaluates the performance of positioning and time-frequency transfer of double-, triple-, quad- and five-frequency PPP models, focusing on the comparison of results among different PPP models. Increasing the length of observations has no obvious practical significance and has little effect; the observations selected in our study can fully support our conclusions. The application of Galileo multi-frequency PPP solutions during different ionospheric active periods requires further investigation.

5. Conclusions

In this contribution, the mathematical PPP model of Galileo five-frequency observations is established; observation types, combination coefficients, ionospheric coefficients, and noise amplification coefficients from the DF to FF PPP models are also compared.

Ranging from 464.6 km to 5991.2 km in four time-frequency links, there are seven-day observations from stations BRUX, CEBR, PTBB, ROAG and USN7 of the MGEX network. GBM, WUM and GRG precise orbits and clock products are used to evaluate the positioning performance and time-frequency transfer stability of the Galileo DF, TF, QF and FF PPP models.

Compared with the DF observation combination, although the multifrequency observation combination reduces noise and increases the redundancy and reliability of the observation equation, the positioning and time-frequency transfer performance are not significantly improved. The average 3D RMS values of the DF, TF, QF and FF1 PPP models are 1.88 cm, 1.95 cm, 1.85 cm, and 1.78 cm, respectively; and the average frequency stabilities of 120,000 s are 1.23×10^{-15} , 1.15×10^{-15} , 1.23×10^{-15} , and 1.23×10^{-15} , respectively. The differences in 3D RMS among the DF, TF, QF and FF1 PPP models are within 0.17 cm, and the differences in frequency stabilities are within 0.08×10^{-15} . The performances of FF1, FF2, FF3, FF4 and UC PPP are also consistent with each other, the differences in 3D RMS values among the FF1, FF2, FF3, FF4 and UC PPP models are within 0.12 cm, and the differences in the frequency stabilities are within 0.02×10^{-15} .

When using WUM and GRG precise products, the differences among the DF, TF, QF and FF PPP models in both positioning and time-frequency transfer performances are quite small, which is consistent with the results obtained using GBM products. The average convergence time obtained using the WUM product is the longest (22.2 min) and that which was achieved using the GRG product is the shortest (15.7 min). Using the GBM, WUM and GRG products, the average 3D RMS values are 1.82 cm, 1.85 cm, and 1.77 cm, respectively, and the average frequency stabilities at 120,000 s are better than 1.18×10^{-15} , 1.13×10^{-15} and 1.06×10^{-15} , respectively. These results show that the PPP performance using the GRG product is slightly better than that of GBM and WUM products, especially in terms of the long-term frequency stability of the BRUX-UN7 link.

Author Contributions: Conceptualization, W.X. and W.-B.S.; methodology, W.X.; software, W.X.; validation, W.X., C.-H.C. and L.-H.L.; formal analysis, W.X., W.-B.S. and L.W.; investigation, W.X. and W.-B.S.; writing—original draft preparation, W.X.; writing—review and editing, W.X., W.-B.S., C.-H.C., L.-H.L., L.W. and Z.-Y.S.; visualization, W.X.; supervision, W.-B.S.; project administration, W.-B.S. All authors have read and agreed to the published version of the manuscript.

Funding: This work was funded by National Natural Science Foundations of China (Grant Nos. 41631072, 42030105, 41721003, 41804012, 41874023), Space Station Project (2020) (Grant No. 228), and the Natural Science Foundation of Hubei Province of China (Grant No. 2019CFB611).

Institutional Review Board Statement: Not applicable.

Informed Consent Statement: Not applicable.

Data Availability Statement: The Galileo observation data from MGEX networks are available at <https://gdc.cddis.eosdis.nasa.gov/gps/data/daily/> (accessed on 24 July 2021). The precise orbit and clock products from are available at <https://gdc.cddis.eosdis.nasa.gov/gps/products/mgex/> (accessed on 24 July 2021). The DCBs are provided at the <ftp://ftp.gipp.org.cn/product/dcb/mgex/> (accessed on 24 July 2021).

Acknowledgments: We gratefully acknowledge the IGS MGEX for providing Galileo observation data. We also acknowledge the WHU, GFZ and CNES for providing precise orbit and clock products.

Conflicts of Interest: The authors declare no conflict of interest.

References

1. Hein, G.W. Status, perspectives and trends of satellite navigation. *Satell. Navig.* **2020**, *1*, 22. [[CrossRef](#)]
2. Montenbruck, O.; Hugentobler, U.; Dach, R.; Steigenberger, P.; Hauschild, A. Apparent clock variations of the Block IIF-1 (SVN62) GPS satellite. *GPS Solut.* **2012**, *16*, 303–313. [[CrossRef](#)]
3. Yang, Y.; Mao, Y.; Sun, B. Basic performance and future developments of BeiDou global navigation satellite system. *Satell. Navig.* **2020**, *1*, 1. [[CrossRef](#)]

4. Zaminpardaz, S.; Teunissen, P.J.G.; Nadarajah, N. GLONASS CDMA L3 ambiguity resolution and positioning. *GPS Solut.* **2016**, *21*, 535–549. [[CrossRef](#)]
5. Wang, K.; Chen, P.; Zaminpardaz, S.; Teunissen, P.J.G. Precise regional L5 positioning with IRNSS and QZSS: Stand-alone and combined. *GPS Solut.* **2018**, *23*, 10. [[CrossRef](#)]
6. Diessongo, T.H.; Schüller, T.; Junker, S. Precise position determination using a Galileo E5 single-frequency receiver. *GPS Solut.* **2013**, *18*, 73–83. [[CrossRef](#)]
7. Su, K.; Jin, S.; Jiao, G. Assessment of multi-frequency global navigation satellite system precise point positioning models using GPS, BeiDou, GLONASS, Galileo and QZSS. *Meas. Sci. Technol.* **2020**, *31*, 064008. [[CrossRef](#)]
8. Chen, J.; Yue, D.; Zhu, S.; Liu, Z.; Zhao, X.; Xu, W. A new cycle slip detection and repair method for Galileo four-frequency observations. *IEEE Access* **2020**, *8*, 56528–56543. [[CrossRef](#)]
9. Zhao, D.; Roberts, G.W.; Hancock, C.M.; Lau, L.; Bai, R. A triple-frequency cycle slip detection and correction method based on modified HMW combinations applied on GPS and BDS. *GPS Solut.* **2019**, *23*, 22. [[CrossRef](#)]
10. Geng, J.; Bock, Y. Triple-frequency GPS precise point positioning with rapid ambiguity resolution. *J. Geod.* **2013**, *87*, 449–460. [[CrossRef](#)]
11. Geng, J.; Guo, J. Beyond three frequencies: An extendable model for single-epoch decimeter-level point positioning by exploiting Galileo and BeiDou-3 signals. *J. Geod.* **2020**, *94*, 14. [[CrossRef](#)]
12. Zhang, P.; Tu, R.; Gao, Y.; Liu, N.; Zhang, R. Improving Galileo's carrier phase time transfer based on prior constraint information. *J. Navig.* **2018**, *72*, 121–139. [[CrossRef](#)]
13. Petit, G. Sub- 10^{-16} accuracy GNSS frequency transfer with IPPP. *GPS Solut.* **2021**, *25*, 22. [[CrossRef](#)]
14. Leute, J.; Petit, G.; Exertier, P.; Samain, E.; Rovera, D.; Uhrich, P. High accuracy continuous time transfer with GPS IPPP and T2L2. In Proceedings of the 2018 European Frequency and Time Forum (EFTF), Turin, Italy, 10–12 April 2018; pp. 249–252.
15. Tavella, P.; Petit, G. Precise time scales and navigation systems: Mutual benefits of timekeeping and positioning. *Satell. Navig.* **2020**, *1*, 10. [[CrossRef](#)]
16. Dow, J.M.; Neilan, R.E.; Rizos, C. The International GNSS Service in a changing landscape of Global Navigation Satellite Systems. *J. Geod.* **2009**, *83*, 191–198. [[CrossRef](#)]
17. Duong, V.; Harima, K.; Choy, S.; Laurichesse, D.; Rizos, C. Assessing the performance of multi-frequency GPS, Galileo and BeiDou PPP ambiguity resolution. *J. Spat. Sci.* **2019**, *65*, 61–78. [[CrossRef](#)]
18. Tu, R.; Liu, J.; Zhang, R.; Zhang, P.; Huang, X.; Lu, X. RTK model and positioning performance analysis using Galileo four-frequency observations. *Adv. Space Res.* **2019**, *63*, 913–926. [[CrossRef](#)]
19. Liu, X.; Jiang, W.; Chen, H.; Zhao, W.; Huo, L.; Huang, L.; Chen, Q. An analysis of inter-system biases in BDS/GPS precise point positioning. *GPS Solut.* **2019**, *23*, 116. [[CrossRef](#)]
20. Qin, W.; Ge, Y.; Wei, P.; Dai, P.; Yang, X. Assessment of the BDS-3 on-board clocks and their impact on the PPP time transfer performance. *Measurement* **2020**, *153*, 107356. [[CrossRef](#)]
21. Li, X.; Liu, G.; Li, X.; Zhou, F.; Feng, G.; Yuan, Y.; Zhang, K. Galileo PPP rapid ambiguity resolution with five-frequency observations. *GPS Solut.* **2019**, *24*, 24. [[CrossRef](#)]
22. Zhang, P.; Tu, R.; Gao, Y.; Zhang, R.; Han, J. Performance of Galileo precise time and frequency transfer models using quad-frequency carrier phase observations. *GPS Solut.* **2020**, *24*, 40. [[CrossRef](#)]
23. Liu, T.; Jiang, W.; Laurichesse, D.; Chen, H.; Liu, X.; Wang, J. Assessing GPS/Galileo real-time precise point positioning with ambiguity resolution based on phase biases from CNES. *Adv. Space Res.* **2020**, *66*, 810–825. [[CrossRef](#)]
24. Kuang, K.; Li, J.; Zhang, S. Galileo real-time orbit determination with multi-frequency raw observations. *Adv. Space Res.* **2021**, *67*, 3147–3155. [[CrossRef](#)]
25. Su, K.; Jin, S. Analytical performance and validations of the Galileo five-frequency precise point positioning models. *Measurement* **2021**, *172*, 108890. [[CrossRef](#)]
26. Jin, S.; Su, K. PPP models and performances from single- to quad-frequency BDS observations. *Satell. Navig.* **2020**, *1*, 16. [[CrossRef](#)]
27. Ge, Y.; Cao, X.; Shen, F.; Yang, X.; Wang, S. BDS-3/Galileo time and frequency transfer with quad-frequency precise point positioning. *Remote Sens.* **2021**, *13*, 2704. [[CrossRef](#)]
28. Leick, A.; Rapoport, L.; Tatarnikov, D. *GPS Satellite Surveying*, 4th ed.; John Wiley & Sons: New York, NY, USA, 2015; pp. 1–807.
29. Liu, T.; Chen, H.; Chen, Q.; Jiang, W.; Laurichesse, D.; An, X.; Geng, T. Characteristics of phase bias from CNES and its application in multi-frequency and multi-GNSS precise point positioning with ambiguity resolution. *GPS Solut.* **2021**, *25*, 58. [[CrossRef](#)]
30. Li, X.; Li, X.; Liu, G.; Feng, G.; Yuan, Y.; Zhang, K.; Ren, X. Triple-frequency PPP ambiguity resolution with multi-constellation GNSS: BDS and Galileo. *J. Geod.* **2019**, *93*, 1105–1122. [[CrossRef](#)]
31. Zhao, L.; Ye, S.; Song, J. Handling the satellite inter-frequency biases in triple-frequency observations. *Adv. Space Res.* **2017**, *59*, 2048–2057. [[CrossRef](#)]
32. Zhang, B.; Teunissen, P.J.; Yuan, Y.; Zhang, H.; Li, M. Joint estimation of vertical total electron content (VTEC) and satellite differential code biases (SDCBs) using low-cost receivers. *J. Geod.* **2018**, *92*, 401–413. [[CrossRef](#)]
33. Petit, G.; Luzum, B. *IERS Conventions (2010)*; IERS Technical Note No. 36; Bureau International des Poids et Mesures Sevres: Frankfurt am Main, Germany, 2010.
34. Kouba, J. *A Guide to Using International GNSS Service (IGS) Products*; Jet Propulsion Laboratory: Pasadena, CA, USA, 2009; p. 34.

35. Wu, J.-T.; Wu, S.C.; Hajj, G.A.; Bertiger, W.I.; Lichten, S.M. Effects of antenna orientation on GPS carrier phase. In Proceedings of the Astrodynamics 1991, San Diego, CA, USA, 19–22 August 1991; pp. 1647–1660.
36. Lyard, F.; Lefevre, F.; Letellier, T.; Francis, O. Modelling the global ocean tides: Modern insights from FES2004. *Ocean Dyn.* **2006**, *56*, 394–415. [[CrossRef](#)]
37. Saastamoinen, J. Contributions to the theory of atmospheric refraction. *Bull. Géodésique (1946–1975)* **1973**, *107*, 13–34. [[CrossRef](#)]
38. Böhm, J.; Heinkelmann, R.; Schuh, H. Short note: A global model of pressure and temperature for geodetic applications. *J. Geod.* **2007**, *81*, 679–683. [[CrossRef](#)]
39. Böhm, J.; Niell, A.; Tregoning, P.; Schuh, H. Global Mapping Function (GMF): A new empirical mapping function based on numerical weather model data. *Geophys. Res. Lett.* **2006**, *33*, 3–6. [[CrossRef](#)]
40. Ge, Y.; Ding, S.; Qin, W.; Zhou, F.; Wang, S. Performance of ionospheric-free PPP time transfer models with BDS-3 quad-frequency observations. *Measurement* **2020**, *160*, 107836. [[CrossRef](#)]